Tunable Fano Resonance and Plasmon–Exciton Coupling in Single Au Nanotriangles on Monolayer WS_2 at Room Temperature

Mingsong Wang, Alex Krasnok, Tianyi Zhang, Leonardo Scarabelli, He Liu, Zilong Wu, Luis M. Liz-Marzán, Mauricio Terrones, Andrea Alù,* and Yuebing Zheng**

Tunable Fano resonances and plasmon–exciton coupling are demonstrated at room temperature in hybrid systems consisting of single plasmonic nanoparticles deposited on top of the transition metal dichalcogenide monolayers. By using single Au nanotriangles (AuNTs) on monolayer WS_2 as model systems, Fano resonances are observed from the interference between a discrete exciton band of monolayer WS_2 and a broadband plasmonic mode of single AuNTs. The Fano lineshape depends on the exciton binding energy and the localized surface plasmon resonance strength, which can be tuned by the dielectric constant of surrounding solvents and AuNT size, respectively. Moreover, a transition from weak to strong plasmon–exciton coupling with Rabi splitting energies of 100–340 meV is observed by rationally changing the surrounding solvents. With their tunable plasmon–exciton interactions, the proposed WS_2–AuNT hybrids can open new pathways to develop active nanophotonic devices.

Plasmon–exciton systems have attracted strong interest as platforms for studying light–matter interactions through mechanisms such as Fano interference,[1–7] strong coupling,[8–13] plasmon-induced resonance energy transfer,[14–16] plasmon-enhanced absorption and emission.[17–19] In particular, Fano resonances and Rabi splitting phenomena in plasmon–exciton systems are promising for the development of new optical devices, including nanolasers, biosensors, and single-photon switches.[4,5,20,21] So far, both Fano resonances and Rabi splitting have been observed in plasmonic systems incorporating dye molecules[8–12,22,23] and quantum dots (QDs).[2–4,24] Due to the lack of efficient ways to tune the excitonic

M. Wang, Z. Wu, Prof. Y. Zheng
Department of Mechanical Engineering
Materials Science and Engineering Program
Texas Materials Institute
The University of Texas at Austin
Austin, TX 78712, USA
E-mail: zheng@austin.utexas.edu

Dr. A. Krasnok, Prof. A. Alù
Department of Electrical and Computer Engineering
The University of Texas at Austin
Austin, TX 78712, USA
E-mail: akrasnok@utexas.edu; alu@mail.utexas.edu

T. Zhang, Prof. M. Terrones
Department of Materials Science and Engineering
The Pennsylvania State University
University Park, PA 16802, USA

Dr. L. Scarabelli, Prof. L. M. Liz-Marzán
Bionanoplasmonics Laboratory
CIC biomaGUNE
Paseo de Miramón 182, 20014 Donostia-San Sebastián, Spain

Dr. L. Scarabelli
Department of Chemistry and Biochemistry
California NanoSystems Institute
University of California
Los Angeles, Los Angeles, CA 90095, USA

The ORCID identification number(s) for the author(s) of this article can be found under https://doi.org/10.1002/adma.201705779.

DOI: 10.1002/adma.201705779

H. Liu, Prof. M. Terrones
Department of Chemistry
The Pennsylvania State University
University Park, PA 16802, USA

Prof. L. M. Liz-Marzán
Ikerbasque
Basque Foundation for Science
48013 Bilbao, Spain

Prof. L. M. Liz-Marzán
Biomedical Research Networking Center in Bioengineering
Biomaterials, and Nanomedicine
CIBER-BBN
20014 Donostia-San Sebastián, Spain

Prof. M. Terrones
Department of Physics and Center for 2-Dimensional
and Layered Materials
The Pennsylvania State University
University Park, PA 16802, USA

Prof. M. Terrones
Department of Materials Science and Engineering
& Chemical Engineering
Carlos III University of Madrid
Avenida Universidad 30, 28911 Leganés, Madrid, Spain

Prof. M. Terrones
IMDEA Materials Institute
Eric Kandel 2, Getafe, Madrid 28005, Spain

© 2018 WILEY-VCH Verlag GmbH & Co. KGaA, Weinheim

properties of the dye molecules and QDs, active control of Fano interference and plasmon–exciton coupling relies on varying surface plasmons or incident light, which has limited the degree of control of Fano asymmetric lineshape and coupling strength to specific light wavelengths and polarizations.[8–12,25–32] In addition, it remains unclear how to distinguish Fano interference and Rabi splitting in such plasmon–exciton systems.

Semiconducting transition metal dichalcogenide (TMDC) monolayers exhibit excitonic properties that can be tuned by external signals, such as electrical bias and temperature.[33–35] Different from dye molecules and QDs, TMDC monolayers possess excitons highly confined in the in-plane direction, thus making it convenient to align the orientation of excitons with the one of surface plasmons for effective dipole–dipole interactions.[16] We propose that these unique features of TMDC monolayers, combined with their other exceptional physical and chemical properties, make hybrid systems of TMDC monolayers and plasmonic NPs ideal platforms for studying tunable Fano resonances and plasmon–exciton coupling.[35–39]

Herein, we report tunable Fano resonances and plasmon–exciton coupling in atomically thin WS_2–AuNT hybrids (schematically shown in **Figure 1**a) at room temperature. Tuning was then demonstrated by active control of the WS_2 exciton binding energy and dipole–dipole interaction. Single-nanoparticle measurements were employed to avoid inhomogeneous spectral broadening brought by ensemble measurements.

We first synthesized monolayer WS_2 by chemical vapor deposition (CVD) and transferred the as-grown monolayer flakes onto a glass substrate (see further information in the Supporting Information).[40] Figure 1b shows an optical image of a representative WS_2 flake on the substrate. The monolayer nature of the WS_2 flake was confirmed by the optical contrast and the strong photoluminescence (PL) signal (Figure 1c), which is typical of direct bandgap semiconductors.[41] The PL spectrum at 300 K under ambient conditions shows a single intense peak centered at 630 nm (1.97 eV), which matches the reported exciton emission of CVD-grown monolayer WS_2.[42] The monolayer nature of CVD-grown WS_2 was further verified by atomic force microscopy (Figure S1, Supporting Information). We further examined the degree of crystallinity of the monolayer WS_2 by measuring the Raman scattering spectrum with a 488 nm excitation laser (Figure 1c). The Raman spectrum is dominated by three peaks at 352, 360, and 421 cm^{-1}, which correspond to the second-order longitudinal acoustic 2LA(M) mode, the first-order out-of-plane E′ mode, and the first-order in-plane A'_1 mode of monolayer WS_2, respectively.[43,44] Colloidal Au nanotriangles (AuNTs) with edge lengths of 60 and 150 nm (referred to as 60 and 150 nm AuNTs) and thickness of 30 nm were synthesized by a previously reported method.[45] The obtained AuNTs have atomically flat surfaces, major in-plane dipoles, and strong E-field enhancement at the tip positions,

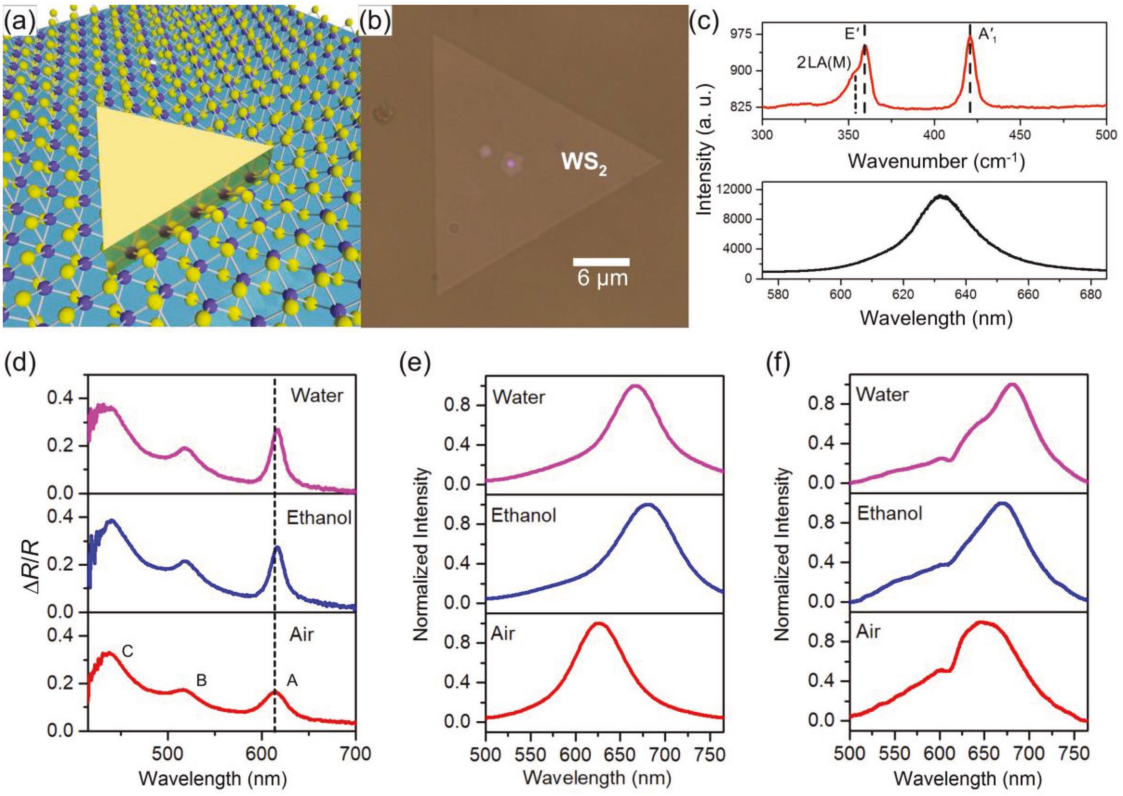

Figure 1. a) Schematic view of a sample comprising a single AuNT on monolayer WS_2. b) Optical image of triangular WS_2 monolayer. c) Raman (top) and PL (bottom) spectra of the monolayer WS_2 in air (the excitation wavelength is 488 nm). d) Vis–NIR differential reflectance spectra of the monolayer WS_2 immersed in air, ethanol, and water. A, B, and C label peaks of exciton A, B, and C, respectively. e) Scattering spectra of a single 60 nm AuNT in air, ethanol, and water. f) Scattering spectra of a single 60 nm AuNT on the monolayer WS_2 in air, ethanol, and water.

© 2018 WILEY-VCH Verlag GmbH & Co. KGaA, Weinheim

as described in the Supporting Information. Transmission electron microscopy was used to image the 60 and 150 nm AuNTs as shown in Figure S2 (Supporting Information).

We hypothesize that Fano resonances may arise from the interference between the discrete exciton band of monolayer WS_2 and the broad plasmonic mode of an individual AuNT.[4,5,46,47] Due to the low dielectric screening, the exciton binding energy of monolayer WS_2 can be tuned by the dielectric constant of the surrounding environment at room temperature.[48,49] Thus, we hypothesized that it should be possible to dynamically control Fano interference and plasmon–exciton coupling in the hybrids consisting of monolayer WS_2 and AuNTs under ambient conditions, by simply changing the surrounding solvents. It should be mentioned that when dealing with the dielectric screening in monolayer WS_2, the static dielectric constant instead of the permittivity at optical frequencies of the surrounding solvents should be considered.[48,49]

In order to verify our hypothesis, we used an optical microscope integrated with a spectrometer and an EMCCD camera to measure reflectance and dark-field scattering spectra from a series of samples (see details in the Supporting Information).[13,16] The differential reflectance spectra of the monolayer WS_2 in different solvents are shown in Figure 1d. Monolayer WS_2 in air has an obvious peak around 615 nm (known as exciton A (neutral exciton), 2.02 eV). The two peaks at shorter wavelengths correspond to excitons B and C.[50] The peak of exciton A red-shifts as the dielectric constant of the solvent increases (Figure 1d), in agreement with previous reports.[48,49] Ethanol and water were chosen because of their large dielectric constants (25.3 and 80.1, respectively) that in turn lead to a large variation of exciton binding energies.[48,49]

We then studied the 60 nm AuNTs on the monolayer WS_2 in different environments (i.e., air, ethanol, and water). The 60 nm AuNTs exhibit an LSPR peak wavelength of ≈620 nm in air (Figure 1e). Their E-field enhancement is stronger than the one of 150 nm AnNTs at the exciton A absorption peak wavelength of the monolayer WS_2, when AuNTs are on monolayer WS_2/SiO_2 substrates and in air, ethanol or water (Figures S4 and S5, Supporting Information). Figure 1e shows that the optical scattering peak wavelength of a single 60 nm AuNT (see scanning electron microscopy (SEM) image of the 60 nm AuNT in Figure 3a) on a glass substrate red-shifts when ethanol or water is added to the sample, because of the increased refractive index.[51] The scattering spectra of a WS_2–AuNT hybrid are shown in Figure 1f (see SEM image of the 60 nm AuNT in Figure 3b). In air or ethanol, the scattering spectrum shows a dip at the absorption peak wavelength of the monolayer WS_2. In contrast, an asymmetric Fano spectral shape, which brings an additional shoulder near the scattering peak, was obtained from the hybrids in water.

We employed a theoretical approach to describe the Fano resonance and explain the variations in the observed spectra measured from the WS_2–AuNT hybrids.[52,53] This approach is an expansion of the original Fano model to non-Hermitian systems with sufficient intrinsic dissipative losses.[52,53] The essential part of this approach is that the scattering cross-section spectra $\sigma_{sc}(\omega)$ of a nanostructure supporting dark and bright modes can be expressed in the following form

$$\sigma_{sc}(\omega) = \sigma_{ex}(\omega)\sigma_{pl}(\omega) \tag{1}$$

where the partial multipliers represent an interference between the radiation continuum and a nonradiative (dark) mode $\sigma_{ex}(\omega)$ and the radiation continuum coupled to a (bright) mode $\sigma_{pl}(\omega)$. These coefficients are given by

$$\sigma_{ex}(\omega) = \frac{\left(\frac{\omega^2-\omega_{ex}^2}{2W_{ex}\omega_{ex}}+q\right)^2+b}{\left(\frac{\omega^2-\omega_{ex}^2}{2W_{ex}\omega_{ex}}\right)+1}, \quad \sigma_{pl}(\omega) = \frac{a^2}{\left(\frac{\omega^2-\omega_{pl}^2}{2W_{pl}\omega_{pl}}\right)+1} \tag{2}$$

where ω_{ex}, W_{ex} and ω_{pl}, W_{pl} are the resonant frequency and the half-width of resonance line at half-maximum of the exciton and plasmonic resonances, respectively, q is the Fano asymmetry parameter, b is the damping parameter originating from intrinsic losses, a is the maximal amplitude of the resonance. We note that Equation (2) assumes $W_{ex} << \omega_{ex}$. It then follows that the Fano resonance results from the competition between the two modes, and thus the Fano lineshape depends on the coupling between the relative dipole strengths. The quantity q represents this relative strength and can be deduced from Fano's original theory[54,55]

$$q = \frac{1}{\pi L_{pl} g} \times \frac{D_{ex}}{d_{pl}} \tag{3}$$

where L_{pl} is the electromagnetic density of states at the plasmon resonance and g is the coupling strength between the surface plasmon (SP) and the exciton, D_{ex} is the total dipole moment of excitons, and d_{pl} is the dipole moment of the NP at the plasmon resonance. Commonly, the SPs have much stronger dipole moment compared to excitons in TMDC monolayers, which causes $|q| << 1$ in a plasmon–exciton system and the asymmetrical Fano lineshapes are undistinguishable. However, this theoretical modeling indicates that, when the dipole moment of the exciton subsystem (which depends on the number of excitons) is comparable to that of SPs, i.e., $|q| \approx 1$, more distinct asymmetrical Fano lineshapes appear, as shown in **Figure 2**a. Our experimental and simulated data indicate that q is negative in our system and, therefore, we only show this particular case. Figure 2a also demonstrates the behavior of the Fano resonance, which can be deduced from Equations (1) and (2), as we vary the Fano parameter q.

In air, the dipole moment of SPs is stronger than the one of excitons, thus in WS_2–AuNT hybrids the SPs are dominating and $|q| << 1$. When the dielectric constant of the solvent increases, asymmetrical lineshapes appear in the scattering spectra (Figure 1f), which implies that $|q|$ becomes larger and close to 1. In order to understand this spectral change, Equations (1) and (2) were used to fit scattering spectra in Figure 1f. However, it should be noted that the scattering spectra of single AuNTs are not single Lorentzian-like spectra, and instead presented flat shoulders at short wavelengths, which are caused by an additional plasmonic resonance in AuNTs (out-of-plane), excited by light with a large incident angle.[45] Since this additional resonance does not get involved into Fano scattering because of its mismatch with the orientation of exciton transition

© 2018 WILEY-VCH Verlag GmbH & Co. KGaA, Weinheim

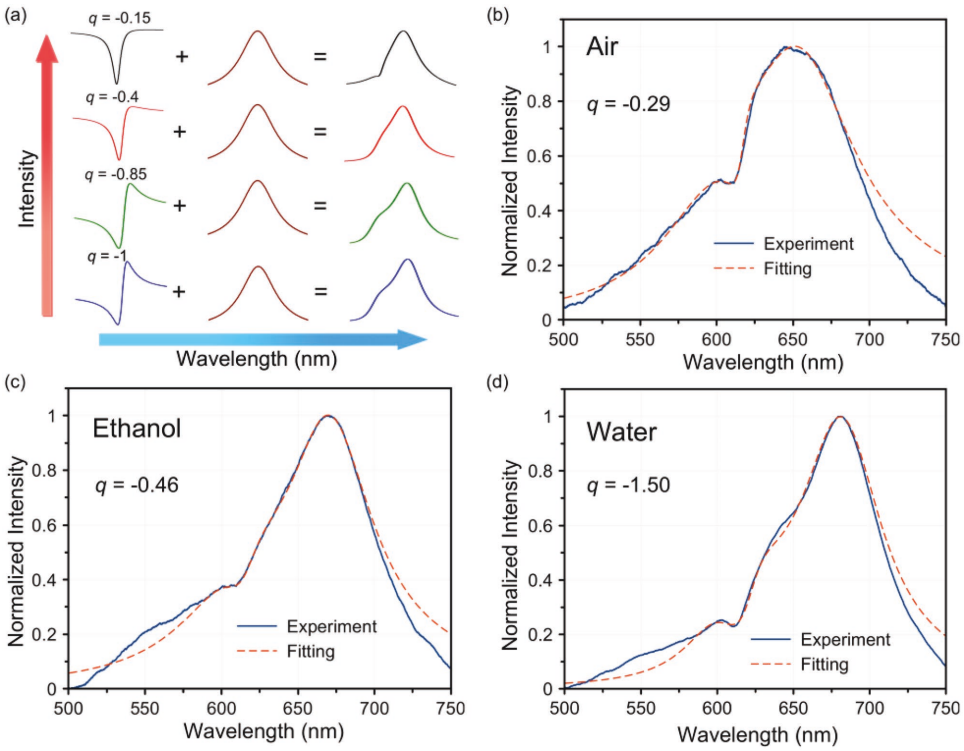

Figure 2. a) Illustration of how Fano lineshape evolves as a function of the asymmetry Fano parameter q. Left curves show the Fano lineshapes for q values of −0.15, −0.4, −0.85, and −1, respectively. The middle curves represent the scattering spectra of single AuNTs. Right curves show the scattering spectra of WS_2–AuNT hybrids for q = −0.15, −0.4, −0.85, and −1, respectively. b–d) Scattering spectra of a single 60 nm AuNT on the monolayer WS_2 in b) air, c) ethanol, and d) water (blue curves), and the results of theoretical analysis (red dashed curves) of the experimentally obtained scattering spectra.

dipoles, we fitted the experimental results (Figure 1f) by adding an additional Lorentzian-like scattering peak to Equation (1). The results of our analysis are summarized in Figure 2b–d (detailed information is provided in Figure S6, Supporting Information). Thus, we conclude that, by increasing the dielectric constant of the solvent, we obtain an increase of $|q|$ from 0.29 (air) to 1.50 (water), while holding its negative value.

The increase in $|q|$ is due to the increase in dipole moment (Equation (3)), which derives from the decrease in exciton binding energy. The exciton binding energy E_b of a 2D excitonic system is given by[56]

$$E_b = 4\frac{m_0 \cdot R_H \cdot a_H^2}{\mu \cdot a_0^2} \quad (4)$$

where m_0 and μ are the free-electron mass and exciton reduced mass, respectively. The parameters R_H, a_H, and a_0 are the Rydberg constant, Bohr radius, and effective Bohr radius, respectively. Since a larger effective Bohr radius represents a larger separation between positive and negative charges, the smaller binding energy leads to a larger dipole moment of excitons. The increase of the exciton dipole moment was verified by the increasing PL intensity when solvents with larger dielectric constant were used (more information is in the Supporting Information).[49] This is because the PL intensity is directly proportional to the square of the total dipole moment of all excitons in the system $D_{ex} \sim d_{ex} \cdot N$, where N is the number of excitons and decreases when the solvent changes from air to water.[57] Note that the differential reflectance spectra demonstrate only slight changes in the bare TMDC light absorption in different solvents, thus indicating that the excitation processes play a minor role in the PL emission enhancement.

From Equation (3), it can be seen that the Fano lineshape also depends on L_{pl} and d_{pl} of SPs, and g between the SP and the excitons. Therefore, changes in plasmonic NPs can tune the Fano lineshape as well. To reveal how this works, we compare 60 nm AuNTs with 150 nm AuNTs (SEM images of 150 nm AuNTs are shown in **Figure 3**c,d). The scattering spectra of 150 nm AuNTs on a glass substrate and on monolayer WS_2 with different solvents are shown in Figure 3e,f respectively. By comparing Figure 3f to Figure 3e no obvious asymmetrical Fano lineshape is observed in the 150 nm AuNT sample. To understand this difference, we compared L_{pl}, g, and d_{pl} of 60 nm AuNTs with those of 150 nm AuNTs. For L_{pl} comparison the numerically calculated normalized local density of states (LDOS) distributions over the AuNTs on SiO_2 substrate are used. The calculation approach we used is outlined in our previous work.[58] The results presented in Figures S8 and S9 (Supporting Information) reveal that both 60 and 150 nm AuNTs exhibit the maximum normalized LDOS of ≈275 at 615 nm nearby their tips (Figure S8, Supporting Information). The normalized LDOS spatial dependance shows that the 60 and 150 nm AuNTs have similar normalized LDOS averaged over AuNTs (Figure S9, Supporting Information). This

© 2018 WILEY-VCH Verlag GmbH & Co. KGaA, Weinheim

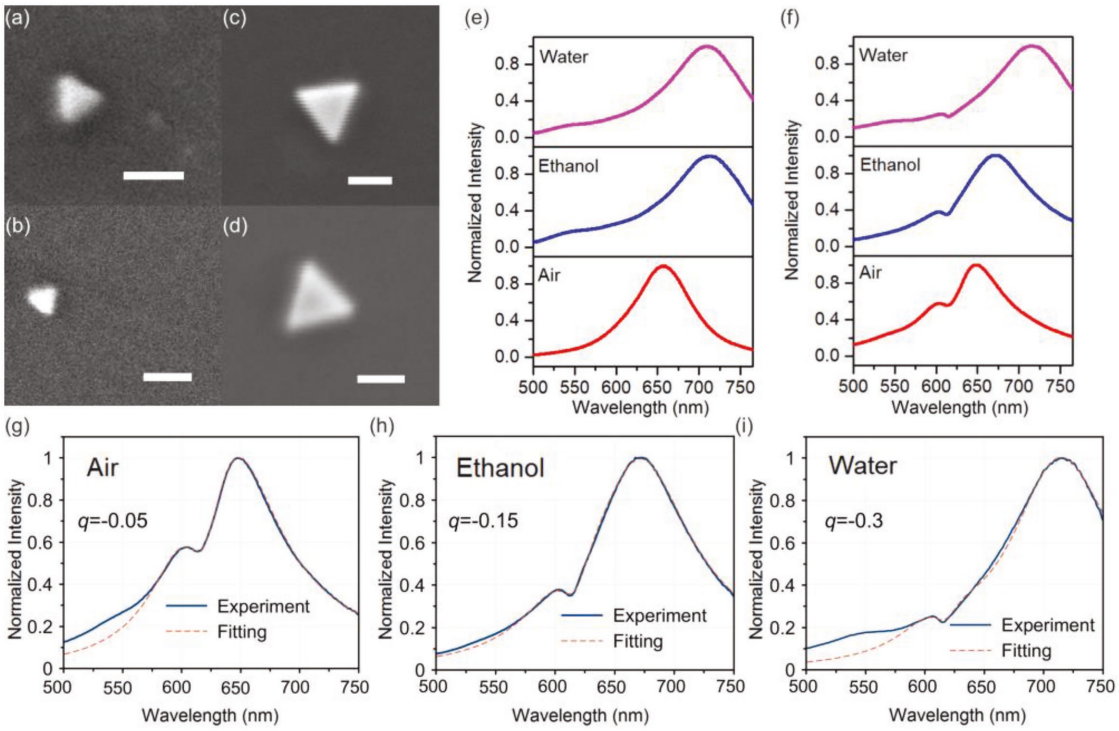

Figure 3. SEM images of a) a 60 nm AuNT on a glass substrate, b) a 60 nm AuNT on monolayer WS_2, c) a 150 nm AuNT on a glass substrate, and d) a 150 nm AuNT on monolayer WS_2. The scale bars are 100 nm. e) Scattering spectra of a single 150 nm AuNT on a glass substrate in air (red curve), ethanol (blue curve), and water (pink curve). f) Scattering spectra of a single 150 nm AuNT on monolayer WS_2 in air (red curve), ethanol (blue curve), and water (pink curve). Scattering spectra (blue curves) and the results of the theoretical analysis (red dashed curves) of the experimentally obtained scattering spectra of a single 150 nm AuNT on the monolayer WS_2 in g) air, h) ethanol, and i) water.

result implies that L_{pl} is approximately the same for 60 and 150 nm AuNTs. As shown in Figures S12 and S13 (Supporting Information), our coupled harmonic oscillator model calculation indicates that, in air and ethanol, the hybrids with 60 nm AuNTs have the smaller g than those with 150 nm AuNTs. However, in water, g for the hybrid with a 60 nm AuNT is ≈1.7 times of that of the hybrid with a 150 nm AuNT. Moreover, the results in Figure S10 (Supporting Information) indicate that 150 nm AuNTs have a larger d_{pl} when compared to 60 nm AuNTs (more than 10 times) with the same solvent. By combining the results of L_{pl}, g, and d_{pl}, we obtain that $|q|$ for 150 nm AuNTs is smaller than that for 60 nm AuNTs. This is consistent with the results obtained from fitting the scattering spectra in Figure 3c, which are shown in Figure 3e–g, (detailed information is in Figure S7, Supporting Information). The fittings show that $|q|$ values for the 150 nm AuNT are 0.05, 0.15, and 0.3 in air, ethanol, and water, respectively, and are all smaller than those for the 60 nm AuNT in the same solvents. It should be mentioned that the LSPR peak wavelength can also be tuned to control the coupling between LSPRs and excitons. For example, Zheng et al. tuned the plasmon–exciton interaction between a silver nanorod and monolayer WSe_2 by varying the thickness of the Al_2O_3 layer that covers the hybrids.[59] The thickness change of the Al_2O_3 layer varies the optical permittivity of the surrounding, which shifts the LSPR peak wavelength of the silver nanorod relative to the exciton peak wavelength of monolayer WSe_2, leading to the changes in the plasmon–exciton coupling and the optical spectra. However, in contrast to our work, the change of the Al_2O_3 layer does not strongly tune the exciton binding energy of the monolayer WSe_2 due to the relatively small dielectric constant of Al_2O_3 (i.e., ≈9),[60] which also explains why there was no obvious asymmetrical Fano lineshape observed in the study by Zheng et al. Our further discussion in the Supporting Information rules out the possibility that the observed spectral changes are derived from the coupling between the high-order plasmonic modes or another possible plasmonic resonances and excitons.

In order to analyze the coupling strength in our system, which cannot be directly obtained from Fano's original theory, we further used the coupled harmonic oscillator model to simulate the scattering spectra.[61,62] For the hybrids with 60 nm AuNTs, we observe that the coupled oscillator model reproduces the experimental results exceptionally well, as shown in Figure S12 (Supporting Information). The important observation is that the coupling strength of the hybrid system increases from 49.63 meV (air) to 169.60 meV (water). Since the coupling strength is determined by the transition dipole moment, the increase in the coupling strength matches the augment of the PL intensity of the monolayer WS_2 from air to water (more discussion is in the Supporting Information). The increase of coupling strength and reduction of dissipative losses of the system when changing the solvent suggest that the strong coupling regime may be achieved in this system. By considering the detuning, the splitting between the upper plexcitonic state (E_+) and the lower plexcitonic state (E_-) equates[63]

© 2018 WILEY-VCH Verlag GmbH & Co. KGaA, Weinheim

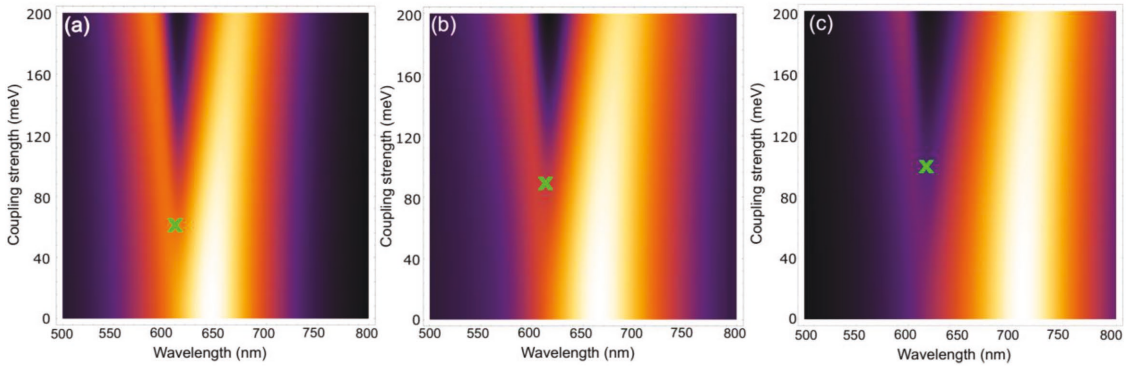

Figure 4. Scattering cross-section dependencies on the wavelength and coupling strength g of the hybrid system with 150 nm AuNTs in a) air, b) ethanol, and c) water. The green crosses show the experimentally achieved values of the coupling strength. The remaining parameters of the systems in different solvents correspond to those of Figure S13 in the Supporting Information.

$$E_+ - E_- = \sqrt{4g^2 + \left(\hbar\delta - i(\hbar W'_{ex} - \hbar W'_{pl})\right)^2} \quad (5)$$

where W'_{ex} is the half-width of resonance line at half-maximum of excitons, W'_{pl} is the half-width of resonance line at half maximum of plasmon resonances, $\hbar$ is the reduced Planck constant, and δ is the detuning that equates $\omega_{pl} - \omega_{ex}$. However, the usually used criterion for the strong coupling-$\hbar\Omega_0 > \hbar W'_{ex} + \hbar W'_{pl}$, where $\hbar\Omega_0$ is Rabi splitting at zero detuning, cannot be directly applied to a system with detuning. Thus an extended criterion is demanded. When the detuning is smaller than ω_{ex}, the splitting of plexcitonic states can be approximately expressed in the form of $\hbar\Omega_0$ through the classic description of strong coupling[64,65] $E_+ - E_- = \sqrt{(\hbar\Omega_0)^2 + \left(\hbar\delta - i(\hbar W'_{ex} - \hbar W'_{pl})\right)^2}$. When $\hbar\Omega_0 > \hbar W'_{ex} + \hbar W'_{pl}$, the system with δ not equating to 0 achieves the strong coupling regime. Hence, we come to conclusion that when $2g > \hbar W'_{ex} + \hbar W'_{pl}$, the system with detuning achieves the strong coupling regime. In our case, this criterion is satisfied only for the system in water, where the $\hbar W'_{ex} + \hbar W'_{pl}$ equals to 153.76 meV, whereas 2 g equals 339.20 meV. Thus, we can conclude that for the hybrid system with 60 nm AuNTs in water, we achieve strong coupling regime, where Rabi splitting sufficiently perturbs the scattering spectrum. The other parameters of the system in different solvents correspond to those shown in Figure S12 (Supporting Information). The corresponding results for 150 nm AuNTs in different solvents are presented in Figure S13 (Supporting Information). For 150 nm AuNTs, the strong coupling is again only achieved in water, where $\hbar W'_{ex} + \hbar W'_{pl}$ and 2 g equal to 182.71 and 198.51 meV, respectively. **Figure 4** and Figure S14 (Supporting Information) demonstrate the dependence of the scattering cross-section on the wavelength and coupling strength g of the hybrid system with 150 and 60 nm AuNTs in air (a), ethanol (b), and water (c), respectively. The green crosses indicate the experimentally achieved values of the coupling strength.

In summary, tunable Fano resonances and plasmon–exciton coupling in the monolayer WS_2–AuNT hybrids have been demonstrated. Fano resonances can be controlled by tuning the exciton binding energy or the LSPR strength through the dielectric constant of surrounding solvents or the dimension of AuNTs. Similarly, a transition from weak to strong plasmon–exciton coupling has been achieved by changing the dielectric constant of surrounding solvents. Large coupling strength of 50–170 meV occur at room temperature due to the strong field localization of the AuNTs and large transition dipole moment of the WS_2 exciton. Our experiments are supported by numerical simulations, which provide a guidance on systematic tuning of the Fano lineshape and Rabi splitting energies. Our demonstrated tunable Fano resonance and Rabi splitting will pave the way toward active devices based on TMDC-plasmonic systems such as optical switches and tunable lasers.[66,67]

Supporting Information

Supporting Information is available from the Wiley Online Library or from the author.

Acknowledgements

Y.Z. acknowledges the financial support of the Office of Naval Research Young Investigator Program (Grant No. N00014-17-1-2424) and the National Science Foundation (Grant No. CBET-1704634). A.A. acknowledges the Air Force Office of Scientific Research MURI Grant No. FA9550-17-1-0002. T.Z. and M.T. acknowledge the financial support from the Army Research Office under MURI grant (W911NF-11-1-0362) and the National Science Foundation (Grant No. 2DARE-EFRI-1433311). L.M.L.-M. acnowledges funding from the Spanish MINECO (Grant No. MAT2013-46101-R).

Conflict of Interest

The authors declare no conflict of interest.

Keywords

Fano resonance, monolayer WS_2, plasmon–exciton coupling, plasmonics, Rabi splitting

Received: October 4, 2017
Revised: March 7, 2018
Published online:

© 2018 WILEY-VCH Verlag GmbH & Co. KGaA, Weinheim

[1] M. Frimmer, T. Coenen, A. F. Koenderink, *Phys. Rev. Lett.* **2012**, *108*, 077404.
[2] W. Zhang, A. O. Govorov, *Phys. Rev. B* **2011**, *84*, 081405.
[3] A. Ridolfo, O. Di Stefano, N. Fina, R. Saija, S. Savasta, *Phys. Rev. Lett.* **2010**, *105*, 263601.
[4] A. E. Miroshnichenko, S. Flach, Y. S. Kivshar, *Rev. Mod. Phys.* **2010**, *82*, 2257.
[5] B. Luk'yanchuk, N. I. Zheludev, S. A. Maier, N. J. Halas, P. Nordlander, H. Giessen, C. T. Chong, *Nat. Mater.* **2010**, *9*, 707.
[6] J. B. Lassiter, H. Sobhani, J. A. Fan, J. Kundu, F. Capasso, P. Nordlander, N. J. Halas, *Nano Lett.* **2010**, *10*, 3184.
[7] R. R. Frontiera, N. L. Gruenke, R. P. Van Duyne, *Nano Lett.* **2012**, *12*, 5989.
[8] J. Bellessa, C. Bonnand, J. C. Plenet, J. Mugnier, *Phys. Rev. Lett.* **2004**, *93*, 036404.
[9] G. A. Wurtz, P. R. Evans, W. Hendren, R. Atkinson, W. Dickson, R. J. Pollard, A. V. Zayats, W. Harrison, C. Bower, *Nano Lett.* **2007**, *7*, 1297.
[10] E.-M. Roller, C. Argyropoulos, A. Högele, T. Liedl, M. Pilo-Pais, *Nano Lett.* **2016**, *16*, 5962.
[11] S. Balci, C. Kocabas, S. Ates, E. Karademir, O. Salihoglu, A. Aydinli, *Phys. Rev. B* **2012**, *86*, 235402.
[12] W. Ni, T. Ambjörnsson, S. P. Apell, H. Chen, J. Wang, *Nano Lett.* **2010**, *10*, 77.
[13] L. Lin, M. Wang, X. Wei, X. Peng, C. Xie, Y. Zheng, *Nano Lett.* **2016**, *16*, 7655.
[14] J. Li, S. K. Cushing, F. Meng, T. R. Senty, A. D. Bristow, N. Wu, *Nat. Photonics* **2015**, *9*, 601.
[15] G. L. Liu, Y.-T. Long, Y. Choi, T. Kang, L. P. Lee, *Nat. Methods* **2007**, *4*, 1015.
[16] M. Wang, B. Bangalore Rajeeva, L. Scarabelli, E. P. Perillo, A. K. Dunn, L. M. Liz-Marzán, Y. Zheng, *J. Phys. Chem. C* **2016**, *120*, 14820.
[17] T. Ming, L. Zhao, Z. Yang, H. Chen, L. Sun, J. Wang, C. Yan, *Nano Lett.* **2009**, *9*, 3896.
[18] M. Wang, G. Hartmann, Z. Wu, L. Scarabelli, B. B. Rajeeva, J. W. Jarrett, E. P. Perillo, A. K. Dunn, L. M. Liz-Marzán, G. S. Hwang, Y. Zheng, *Small* **2017**, *13*, 1701763.
[19] G. M. Akselrod, C. Argyropoulos, T. B. Hoang, C. Ciracì, C. Fang, J. Huang, D. R. Smith, M. H. Mikkelsen, *Nat. Photonics* **2014**, *8*, 835.
[20] R. Chikkaraddy, B. de Nijs, F. Benz, S. J. Barrow, O. A. Scherman, E. Rosta, A. Demetriadou, P. Fox, O. Hess, J. J. Baumberg, *Nature* **2016**, *535*, 127.
[21] V. Giannini, A. I. Fernández-Domínguez, S. C. Heck, S. A. Maier, *Chem. Rev.* **2011**, *111*, 3888.
[22] N. T. Fofang, N. K. Grady, Z. Fan, A. O. Govorov, N. J. Halas, *Nano Lett.* **2011**, *11*, 1556.
[23] B. G. DeLacy, O. D. Miller, C. W. Hsu, Z. Zander, S. Lacey, R. Yagloski, A. W. Fountain, E. Valdes, E. Anquillare, M. Soljačić, S. G. Johnson, J. D. Joannopoulos, *Nano Lett.* **2015**, *15*, 2588.
[24] R. D. Artuso, G. W. Bryant, *Nano Lett.* **2008**, *8*, 2106.
[25] A. E. Schlather, N. Large, A. S. Urban, P. Nordlander, N. J. Halas, *Nano Lett.* **2013**, *13*, 3281.
[26] N. T. Fofang, T.-H. Park, O. Neumann, N. A. Mirin, P. Nordlander, N. J. Halas, *Nano Lett.* **2008**, *8*, 3481.
[27] Y. B. Zheng, B. K. Juluri, L. Lin Jensen, D. Ahmed, M. Lu, L. Jensen, T. J. Huang, *Adv. Mater.* **2010**, *22*, 3603.
[28] W. Ni, Z. Yang, H. Chen, L. Li, J. Wang, *J. Am. Chem. Soc.* **2008**, *130*, 6692.
[29] F. Nan, Y.-F. Zhang, X. Li, X.-T. Zhang, H. Li, X. Zhang, R. Jiang, J. Wang, W. Zhang, L. Zhou, J.-H. Wang, Q.-Q. Wang, Z. Zhang, *Nano Lett.* **2015**, *15*, 2705.
[30] W. Zhang, A. O. Govorov, G. W. Bryant, *Phys. Rev. Lett.* **2006**, *97*, 146804.
[31] G. Zengin, M. Wersäll, S. Nilsson, T. J. Antosiewicz, M. Käll, T. Shegai, *Phys. Rev. Lett.* **2015**, *114*, 157401.
[32] A. Manjavacas, F. J. G. d. Abajo, P. Nordlander, *Nano Lett.* **2011**, *11*, 2318.
[33] Q. H. Wang, K. Kalantar-Zadeh, A. Kis, J. N. Coleman, M. S. Strano, *Nat. Nanotechnol.* **2012**, *7*, 699.
[34] D. Jariwala, V. K. Sangwan, L. J. Lauhon, T. J. Marks, M. C. Hersam, *ACS Nano* **2014**, *8*, 1102.
[35] I. Abid, W. Chen, J. Yuan, A. Bohloul, S. Najmaei, C. Avendano, R. Péchou, A. Mlayah, J. Lou, *ACS Photonics* **2017**, *4*, 1653.
[36] M. Koperski, M. R. Maciej, A. Arora, K. Nogajewski, A. O. Slobodeniuk, C. Faugeras, M. Potemski, *Nanophotonics* **2017**, *6*, 1289.
[37] S. Manzeli, D. Ovchinnikov, D. Pasquier, O. V. Yazyev, A. Kis, *Nat. Rev. Mater.* **2017**, *2*, 17033.
[38] K. F. Mak, J. Shan, *Nat. Photonics* **2016**, *10*, 216.
[39] J. Wen, H. Wang, W. Wang, Z. Deng, C. Zhuang, Y. Zhang, F. Liu, J. She, J. Chen, H. Chen, S. Deng, N. Xu, *Nano Lett.* **2017**, *17*, 4689.
[40] V. Carozo, Y. Wang, K. Fujisawa, B. R. Carvalho, A. McCreary, S. Feng, Z. Lin, C. Zhou, N. Perea-López, A. L. Elías, B. Kabius, V. H. Crespi, M. Terrones, *Sci. Adv.* **2017**, *3*, e1602813.
[41] Y. Zhang, Y. Zhang, Q. Ji, J. Ju, H. Yuan, J. Shi, T. Gao, D. Ma, M. Liu, Y. Chen, X. Song, H. Y. Hwang, Y. Cui, Z. Liu, *ACS Nano* **2013**, *7*, 8963.
[42] C. Cong, J. Shang, X. Wu, B. Cao, N. Peimyoo, C. Qiu, L. Sun, T. Yu, *Adv. Opt. Mater.* **2014**, *2*, 131.
[43] H. Terrones, E. D. Corro, S. Feng, J. M. Poumirol, D. Rhodes, D. Smirnov, N. R. Pradhan, Z. Lin, M. A. T. Nguyen, A. L. Elías, T. E. Mallouk, L. Balicas, M. A. Pimenta, M. Terrones, *Sci. Rep.* **2014**, *4*, 4215.
[44] A. Berkdemir, H. R. Gutiérrez, A. R. Botello-Méndez, N. Perea-López, A. L. Elías, C.-I. Chia, B. Wang, V. H. Crespi, F. López-Urías, J.-C. Charlier, H. Terrones, M. Terrones, *Sci. Rep.* **2013**, *3*, 1755.
[45] L. Scarabelli, M. Coronado-Puchau, J. J. Giner-Casares, J. Langer, L. M. Liz-Marzán, *ACS Nano* **2014**, *8*, 5833.
[46] F. Shafiei, F. Monticone, K. Q. Le, X.-X. Liu, T. Hartsfield, A. Alu, X. Li, *Nat. Nanotechnol.* **2013**, *8*, 95.
[47] C. Argyropoulos, F. Monticone, G. D'Aguanno, A. Alù, *Appl. Phys. Lett.* **2013**, *103*, 143113.
[48] N. Mao, Y. Chen, D. Liu, J. Zhang, L. Xie, *Small* **2013**, *9*, 1312.
[49] Y. Lin, X. Ling, L. Yu, S. Huang, A. L. Hsu, Y.-H. Lee, J. Kong, M. S. Dresselhaus, T. Palacios, *Nano Lett.* **2014**, *14*, 5569.
[50] B. Zhu, X. Chen, X. Cui, *Sci. Rep.* **2015**, *5*, 9218.
[51] J. N. Anker, W. P. Hall, O. Lyandres, N. C. Shah, J. Zhao, R. P. van Duyne, *Nat. Mater.* **2008**, *7*, 442.
[52] B. Gallinet, O. J. F. Martin, *ACS Nano* **2011**, *5*, 8999.
[53] B. Gallinet, O. J. F. Martin, *Phys. Rev. B* **2011**, *83*, 235427.
[54] U. Fano, *Phys. Rev.* **1961**, *124*, 1866.
[55] T.-T. Tang, Y. Zhang, C.-H. Park, B. Geng, C. Girit, Z. Hao, M. C. Martin, A. Zettl, M. F. Crommie, S. G. Louie, Y. R. Shen, F. Wang, *Nat. Nanotechnol.* **2010**, *5*, 32.
[56] H. Mathieu, P. Lefebvre, P. Christol, *Phys. Rev. B* **1992**, *46*, 4092.
[57] D. G. Baranov, R. S. Savelev, S. V. Li, A. E. Krasnok, A. Alù, *Laser Photonics Rev.* **2017**, *11*, 1600268.
[58] A. E. Krasnok, A. P. Slobozhanyuk, C. R. Simovski, S. A. Tretyakov, A. N. Poddubny, A. E. Miroshnichenko, Y. S. Kivshar, P. A. Belov, *Sci. Rep.* **2015**, *5*, 12956.
[59] D. Zheng, S. Zhang, Q. Deng, M. Kang, P. Nordlander, H. Xu, *Nano Lett.* **2017**, *17*, 3809.
[60] J. D. Plummer, P. B. Griffin, *Proc. IEEE* **2001**, *89*, 240.

© 2018 WILEY-VCH Verlag GmbH & Co. KGaA, Weinheim

[61] X. Wu, S. K. Gray, M. Pelton, *Opt. Express* **2010**, *18*, 23633.
[62] G. Zengin, G. Johansson, P. Johansson, T. J. Antosiewicz, M. Käll, T. Shegai, *Sci. Rep.* **2013**, *3*, 3074.
[63] D. G. Baranov, M. Wersäll, J. Cuadra, T. J. Antosiewicz, T. Shegai, *ACS Photonics* **2018**, *5*, 24.
[64] P. Törmä, W. L. Barnes, *Rep. Prog. Phys.* **2015**, *78*, 013901.
[65] C. Tserkezis, M. Wubs, N. A. Mortensen, *ACS Photonics* **2018**, *5*, 133.
[66] C. Argyropoulos, P.-Y. Chen, F. Monticone, G. D'Aguanno, A. Alù, *Phys. Rev. Lett.* **2012**, *108*, 263905.
[67] Z. Sun, A. Martinez, F. Wang, *Nat. Photonics* **2016**, *10*, 227.

© 2018 WILEY-VCH Verlag GmbH & Co. KGaA, Weinheim